Quantifying Global Warming Response of the Orographic Precipitation in a Typhoon Environment with Large-Eddy Simulations

JIANAN CHEN[a] AND XIAOMING SHI[a,b]

[a] *Division of Environment and Sustainability, Hong Kong University of Science and Technology, Hong Kong, China*
[b] *Center for Ocean Research in Hong Kong and Macau, Hong Kong University of Science and Technology, Hong Kong, China*

(Manuscript received 12 January 2023, in final form 28 June 2023, accepted 29 June 2023)

ABSTRACT: The intense and moist winds in a tropical cyclone (TC) environment can produce strong mountain waves and enhanced precipitation over complex terrain, yet few studies have investigated how the orographic precipitation in a TC environment might respond to global warming. Here, we use large-eddy simulation to estimate the global warming–induced change in the precipitation near an idealized mountain (1 km maximum height) with pseudo global warming. Two regions exhibit enhanced precipitation, one over the mountain and the other in the downstream region 25–45 km away from the mountain. The enhanced precipitation in both regions is related to the seeder–feeder mechanism, although the enhancement in the downstream regions differs from the conventional definition and is referred to as the pseudo-seeder–feeder mechanism (PSF). In the PSF, mountain waves generate an intense cloud formation center in the midtroposphere above the lee slope, and the resulting hydrometeors drift downstream, intensifying downstream convection when they fall into proper locations. Under warming, the overmountain precipitation maximum exhibits minimal changes, while the downstream precipitation maximum exhibits a large sensitivity of 18% K^{-1}. The small sensitivity of the first precipitation peak is due to the canceling effects of thermodynamic and dynamic changes. The large sensitivity in the downstream region is mainly due to the strengthening of the wave-induced midtroposphere cloud formation center, which supplies more hydrometeors to the downstream region and enhances precipitation efficiency through the enhanced PSF mechanism. However, the downstream precipitation sensitivity varies with mountain geometry. Higher mountain height enhances precipitation but lowers the sensitivity to warming.

SIGNIFICANCE STATEMENT: The combination of typhoon environment and orography can produce intense precipitation and thereby severe flooding risks. Here, we investigate the global warming response of orographic precipitation in a typhoon environment with idealized, high-resolution simulations. The experiments suggest that under warming, a precipitation maximum may emerge in the downstream region of a mountain or strengthen and shift upwind if it already exists in the current climate. This surprising amplification of downstream-region precipitation is related to the enhancement of the midtropospheric cloud generation caused by mountain waves and has critical implications for flooding risk management in mountainous regions.

KEYWORDS: Mountain waves; Precipitation; Climate change; Orographic effects; Large eddy simulations; Mountain meteorology

1. Introduction

The mountains and their foothills are dwelling places for around 26% of the global population (Beniston 2005). An essential source of water supply in the mountainous region is orographic precipitation (Schär and Frei 2005). Yet, heavy orographic precipitation can also induce flash floods and subsequently bring social and economic damages to human society (Houze 2012). It is therefore of critical importance to assess how the orographic precipitation will change in response to the warming climate.

Global warming can affect orographic precipitation through modification of thermodynamic, dynamic, and cloud microphysics factors. In terms of the thermodynamic factors, with roughly unchanged relative humidity, the water vapor in the atmosphere will increase by ~7% K^{-1} of surface warming based on the thermodynamic Clausius–Clapeyron (CC) equation (O'Gorman 2015). The increased moisture in a warmed climate is expected to increase precipitation over mountains. For example, Jing et al. (2019) show that in their pseudo global warming simulations, the projected increase of wintertime precipitation in the interior western United States mountains under global warming is mainly induced by increased moisture with other factors playing secondary roles. The dry ratio, which measures the fraction of incoming water mass being removed by orographic precipitation, was found to decrease with warming primarily due to the slower change in moist adiabatic lapse rate compared to that of saturation vapor pressure (Kirshbaum and Smith 2008). The thermodynamics can also lead to an upward shift of the windward condensation center because the fractional change in condensation increases with height (Siler and Roe 2014). For the dynamic factors, the increased temperature and moisture can alter the gravity wave dynamics, which can further affect the precipitation.

Supplemental information related to this paper is available at the Journals Online website: https://doi.org/10.1175/JCLI-D-23-0018.s1.

Corresponding author: Xiaoming Shi, shixm@ust.hk

DOI: 10.1175/JCLI-D-23-0018.1

Shi and Durran (2015) conducted an idealized study to investigate the orographic precipitation over idealized north–south-oriented midlatitude mountain barriers and found that the extreme precipitation over the eastern slope increases at a rate higher than that over the western slope. The relatively strong response over the eastern slope is explained by the vertical velocity change, which is governed by gravity wave dynamics. In addition, large-scale circulation shifts under warming can affect where the precipitation forms through the moisture transport (Shi and Durran 2014). The warming response of microphysical processes occurring in clouds has been investigated in several studies (Kirshbaum et al. 2018). Kirshbaum and Smith (2008) found that precipitation efficiency (PE) will decrease in response to warming because the mixed-phase rain processes are partly replaced by the less efficient warm rain process. Pavelsky et al. (2012) show that the lifted freezing level in a warmed climate may cause an upwind shift of orographic distribution. With a higher freezing level, falling hydrometeors from upper levels will shift earlier from solid phase to liquid phase. Considering the faster falling speed of liquid hydrometeors, the hydrometeors will fall in a shorter distance and therefore cause an upwind shift in the precipitation distribution (Pavelsky et al. 2012).

Some of the most intense precipitation events happen when tropical cyclones (TCs) pass over complex terrain (Houze 2012; Smith et al. 2009). A TC can produce heavy rainfall directly in its spiral rainband and eyewall, or indirectly through the interaction between its circulation with mountain ranges (Wang et al. 2009). When a steep mountain range intersects with TC circulation, the environmental conditions featuring strong surface wind, moist air, and low static stability are consistent with empirical conditions favoring the occurrence of intense orographic precipitation (Lin et al. 1998). However, previous research has not investigated how the orographic precipitation induced by the interaction between mountain range and TC outer region circulation will change in response to warming. This might be due to two reasons. First, it is computationally infeasible to simulate a TC spanning thousands of kilometers horizontally with large-eddy simulation (LES) resolution that can explicitly resolve the fine-scale process (Bryan et al. 2017). The use of convection parameterization is often accused of being the reason for inconsistent prediction of extreme precipitation sensitivities to warming in climate models (Muller 2013; O'Gorman 2015). To avoid the uncertainties brought by the convection parameterization schemes, convection-permitting models with horizontal grid spacings on the order of one kilometer have been employed to investigate the warming response of convective systems (Guichard and Couvreux 2017; Kirshbaum and Smith 2008). However, the kilometer-scale resolution is in the gray zone of convection and terrain (for smaller mountains) and how to resolve gray zone issues is an ongoing topic (Chow et al. 2019). LES can help avoid those uncertain issues, but it is computationally demanding to conduct three-dimensional typhoon simulations at the resolution of ~100 m. Second, a direct comparison is hard to achieve because TC outer region rainband is highly asymmetric. Therefore, even in pseudo global warming experiments (Schär et al. 1996; Trapp et al. 2021), it is difficult to ensure the same timing for a preexisting convective system or moisture plume to impinge on a mountain. As a result, it is hard to tell whether orographic precipitation differences in the experiments are due to warming or timing (i.e., preexisting convective system may impinge onto the mountain at different stages of the life cycle of the system).

To overcome those difficulties, we adopted the LES method developed by Bryan et al. (2017, hereafter B17) to simulate the TC environment. Instead of simulating the entire TC, this LES method only simulates a small "patch" of a typhoon. The large-scale conditions that dominate the small patch are specified using prescribed input parameters. Therefore, the large-scale conditions can be controlled to ensure direct comparisons. The warming experiments of the LES simulations are conducted with the pseudo global warming method (Rasmussen et al. 2011; Sato et al. 2007; Takemi et al. 2016). We will focus on the intensity and distribution changes in orographic precipitation due to warming and investigate the underlying mechanisms.

2. Experiment setup

a. *Typhoon case*

The large-eddy simulations have an idealized environment based on a real typhoon event. We focus on a typhoon's outer region environment featuring strong wind and highly moist condition. The wind field in this environment is subject to centrifugal force and mesoscale advection tendencies associated with the low pressure center of the typhoon (Bryan et al. 2017). Typhoon Vicente (2012) is one of the strongest typhoons affecting Hong Kong (HK) in recent decades and it caused more than 200 mm of precipitation over the two-day period during its passage over HK (Hong Kong Observatory 2012). According to observation data, the strongest precipitation in HK occurred 12 h after Vicente's landfall when Vicente was more than 300 km away from HK. During the period from 0500 to 0700 UTC 24 July 2012, intense precipitation happened in Hong Kong.

During the 2-h intense precipitation period, Hong Kong happened to be located nearly due east of the cyclone center as indicated by the black square box in Fig. S1 in the online supplemental material. Therefore, for simplicity, no rotation of the wind profile was applied when setting the LES domain, and the tangential wind for the LES domain is assumed to be from due south. The square box in Fig. S1 is centered at the Lantau Island of Hong Kong with a side length of 100 km. The radius from the low pressure center of the typhoon to the square center is 338.84 km. The Weather Research and Forecast (WRF) Model was used to simulate Typhoon Vicente in a previous study (Shi and Wang 2022) with horizontal resolution down to 1.6 km. We use the WRF simulation data to determine the input parameter profiles for base state and initial conditions of our LES, by averaging relevant variables in the small square region in Fig. S1 and over the 2-h period with the most intense precipitation.

b. *LES setup*

For our LES, we use the TC environment parameterization method developed by Bryan et al. (2017) for the nonhydrostatic numerical model Cloud Model 1 (CM1, version 20.3) (Bryan and Fritsch 2002), which is an advanced tool for idealized LES

and convection-permitting simulations. The LES domain consists of $N_x = 256$ grid points in the x direction with $\Delta x = 200$ m and a total length of $L_x = 51.2$ km. In the y direction, there are $N_y = 512$ grid points, with $\Delta y = 200$ m and a total length of $L_y = 102.4$ km. In the vertical direction, the model has $N_z = 128$ levels, with the grid spacing Δz stretching from 150 m near the surface to 500 m at the model top ($L_z = 31.2$ km). We refer to our simulations as LES based on Matheou and Chung (2014) and Shi et al. (2019), who suggested that deep convection requires vertical resolution higher than 530 m and horizontal resolution higher than 300 m to resolve the majority (90%) of eddy kinetic energy. However, it should be noted that controversy exists on what can be called an LES. Several criteria exist for determining whether a simulation is an LES: 1) the existence of a broad and well-defined inertial subrange (e.g., Saddoughi and Veeravalli 1994), 2) sufficient scale separation between energy production and dissipation (e.g., Bryan et al. 2003), 3) convergence of the simulation to finer-resolution results (e.g., Ardeshiri et al. 2020), and 4) resolving the majority of turbulent fluxes as mentioned above.

Our boundary conditions are doubly periodic in the horizontal. The Rayleigh damping is applied at heights above 22 km to avoid the excessive spurious reflection of gravity waves. The research is conducted mainly using the Thompson scheme (Thompson et al. 2008) as the microphysics scheme. For testing robustness of our conclusions, we also conducted some simulations with the Morrison microphysics scheme (Morrison et al. 2009) and documented the results in section 6. For subgrid-scale turbulence parameterization, we used the TKE scheme (Deardorff 1980), and radiation is computed using the Rapid Radiative Transfer Model for general circulation models (RRTMG) (Iacono et al. 2008). For the surface model, surface-layer scheme from WRF model is used. Surface fluxes and surface stress are computed based on the Monin–Obukhov similarity theory with the Carlson-Boland viscous sublayer (Carlson and Boland 1978).

The B17 method was originally designed for simulating the wind profiles in the boundary layer of the outer region in TC. In this study, to investigate the interaction between convections and the mountain, the method is adapted, and the LES domain extends to 31.2 km in height. The TC boundary wind profile simulation model in B17 is based on the assumption that the small LES domain (embedded within the TC environment) is subject to centrifugal and advection accelerations that apply at scales larger than the domain. The fundamental idea of B17 is to account for these large-scale conditions by specifying the vertical profile of gradient wind speed V, the radial gradient of gradient wind speed $\partial V/\partial R$, and a distance away from the tropical cyclone center R. Other than these parameters, to initiate the simulation, the vertical profile of potential temperature (θ), water vapor mixing ratio (q_v) are needed and shown in Fig. 1. B17 suggests that the $\partial V/\partial R$ can be related to V/R through a decay rate n, $\partial V/\partial R = -n(V/R)$. The decay rate n for all types of tropical cyclones ranges from 0.04 to 0.64 (Mallen et al. 2005). We have found that the precipitation intensity and distribution are insensitive to the selection of decay rate in this range. In view of this, a decay rate of 0.6 is used. The distance between the center of our research domain and the low pressure center R is 338.84 km.

The large-scale pressure gradient in B17, originally designed for the atmospheric boundary layer, is derived from the gradient wind balance relationship. However, the gradient wind balance no longer holds at higher levels where there is no well-defined circular low pressure center. Figure 1a shows the profile of meridional velocity V_{WRF} derived from the temporal and spatial mean of V from WRF output data, geostrophic wind V_{GEO} calculated based on the geostrophic balance, and V_{GRAD} calculated from the gradient wind balance. Below $z_1 = 11$ km, V_{WRF} is consistent with V_{GRAD} except at the levels near the surface, suggesting that in the lower and middle troposphere the large-scale wind field is well approximated by the gradient wind balance in which the pressure gradient force is balanced by centrifugal force and Coriolis force. The inconsistency between V_{WRF} and V_{GRAD} at the lowest levels is due to the unaccounted surface friction and boundary layer flux. Above $z_2 = 15.5$ km indicated by the green dotted horizontal line, the V_{WRF} oscillates around zero and shows good agreement with V_{GEO}, suggesting that the wind field follows the geostrophic balance in which the large-scale pressure gradient is balanced only by the Coriolis force. At heights between z_1 and z_2, the wind field transitions from the gradient wind balance to the geostrophic wind balance, in which the centrifugal force gradually disappears.

In our setup of the large-scale pressure gradient in LES, for simplicity, we apply a linear decay coefficient α on the centrifugal force term and assume α decreases from unity at height z_1 to zero at height z_2 to represent the disappearance of centrifugal force. At levels above z_2, with no presence of centrifugal forces, we specify the large-scale pressure gradient force based on the geostrophic wind balance by setting α as 0. In the LES method of B17, mesoscale tendency terms are associated with the mesoscale flows in the tropical cyclone. Similarly, we apply the same decay coefficient α on the mesoscale tendency terms.

The original B17 method focuses on simulations of the wind profiles in the dry atmosphere. Moisture effects are neglected. Similar to Chen et al. (2021), nudging terms are applied to the tendency of temperature, specific humidity, and large-scale wind for the purpose of accounting for the effects of the large-scale circulation of typhoon environment. Details are found in Eqs. (1b) and (1c) from Chen et al. (2021). This nudging approach ensures that the large wind profiles, temperature, and moisture remain anchored throughout the simulations. The nudging relaxation time scale we used is 2 h.

The terrain profile and initial flow field are specified by several parameters. The idealized bell-shaped terrain is set up to loosely mimic the Hong Kong topography, which is characterized by west–east-oriented mountains. The surface elevation Z_s of this bell-shaped mountain is specified as

$$Z_s(y) = \begin{cases} \dfrac{h_0}{2}\left\{1 + \cos\left\{\pi\left[\dfrac{(y - y_m)}{a}\right]\right\}\right\}, & \text{if } y_m - a < y < y_m + a \\ 0, & \text{else} \end{cases}, \tag{1}$$

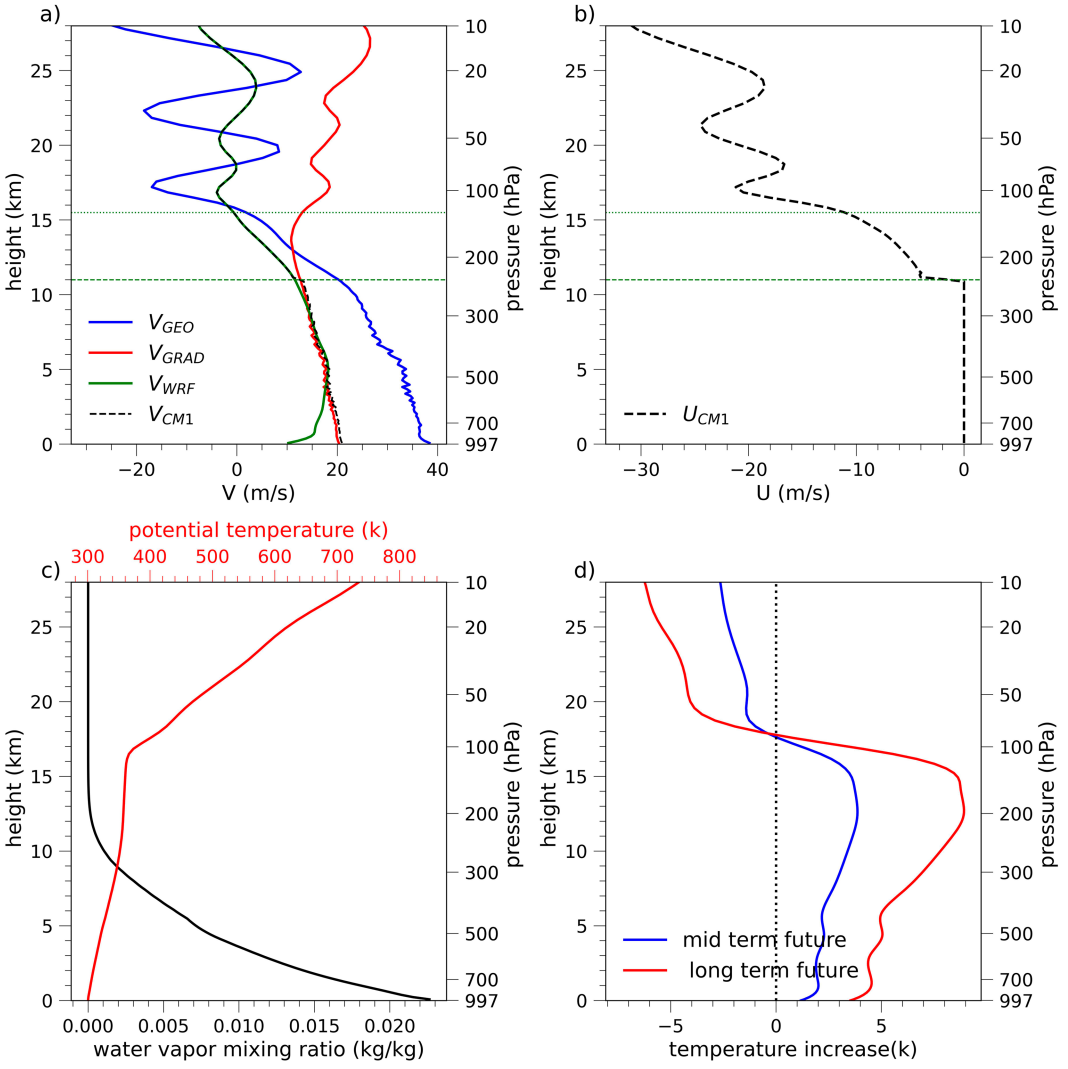

FIG. 1. (a),(b) Vertical profiles of horizontal wind (V and U). The mean V profiles derived directly from the WRF simulation are denoted by the solid green line. The mean V profiles calculated based on the geostrophic wind balance are shown as the solid blue lines and labeled as V_{GEO}. The V profile calculated based on the gradient wind balance is shown as the solid red line and labeled as V_{GRAD}. The dashed black lines show the input V and U profiles used in our simulation and are labeled as V_{CM1} and U_{CM1}, respectively. (c) Potential temperature derived directly from the WRF simulation and water vapor mixing ratio (q_v). The q_v is derived assuming the atmosphere is saturated. (d) The CMIP6-predicted temperature increase of midterm future climate (blue line) and long-term future (red line) relative to present climate.

where the maximum height h_0 is 1 km, the half-width a is 10 km, and $y_m = 0$ is at the center of the domain in the meridional direction. The surface area where $Z_s = 0$ is set as ocean surface. The mountain is symmetric in the zonal x direction.

c. *Warming experiments*

In the warming experiments, we have conducted pseudo global warming by adding the temperature change predicted by the SSP5–8.5 (Shared Socioeconomic Pathway) warming scenario from the Coupled Model Intercomparison Project phase 6 (CMIP6) simulations onto the control simulation temperature profile. The current climate state is defined as the average for the period of 2015–20, the midterm future as the period of 2050–60, and the long-term future as the period of 2090–2100. The temperature is averaged over the larger domain centered at Hong Kong, ranging from 110° to 120°E in longitude and from 15° to 25°N in latitude. The surface warming relative to the present climate is 1.18 and 3.53 K, respectively, for the climate of the midterm future and long-term future. Figure 1d shows temperature change between present climate and future climates. The temperature anomaly profiles are characterized by the strongest warming happening in the upper troposphere, and the cooling happening in the stratosphere, consistent with previous studies (e.g., Ji et al. 2020). In the troposphere, the upper levels exhibit

stronger warming than the low levels, suggesting a more stable atmosphere under warming. In terms of the input of vertical profile of q_v, since the approximately constant relative humidity under global warming is found in both observation (e.g., Douville et al. 2022) and most climate models (e.g., Soden and Held 2006), we assume the relative humidity profile remains constant over the warming. Therefore, we have three groups of simulations: present, midterm future, and long-term future climate. For the simulations of future climate scenarios, we applied the same nudging method except the potential temperature profile is nudged toward the future potential temperature profile, which is the potential temperature profile with superposed mean potential temperature changes based on the climatology in CMIP6 simulations. Relative humidity was assumed to be constant. Each simulation was integrated for 36 h with an output interval of 10 min. The first 12 h are discarded as the spinup period. In the analysis below, unless otherwise specified, the temporal average is taken over the period from hour 12 to hour 36.

3. Orographic precipitation and traveling convective system

a. *Precipitation distributions*

The zonal (x direction) and temporal mean precipitation distributions are shown in Fig. 2. In the simulation of the present climate, two local precipitation maxima can be identified. The first precipitation maximum is located on the lee slope of the mountain and the second precipitation peak is downstream of the mountain at around 37 km. The simulations for midterm future and long-term future climate exhibit qualitatively similar precipitation maxima patterns with peaks on the lee slope and in the downstream region.

The first precipitation peak on the mountain slope barely changes (shown in Fig. 2a) with warming. By contrast, the second downstream-region precipitation peak shifts upwind toward the mountain and intensifies substantially with warming. Figure 2b shows the corresponding precipitation sensitivity, which is defined as the change relative to the present climate, normalized by surface temperature increase. The sensitivity near the first peak is close to zero. However, the precipitation sensitivity related to the second precipitation maximum has shown large sensitivity and can reach up to 34.65% K^{-1} in the midterm future and up to 43.41% K^{-1} in the long-term future.

b. *Mean state of present climate simulations*

The mean states of the present climate simulations are investigated to identify and explain essential mechanisms involved in shaping the distribution pattern of precipitation in our simulations. Figure 3a shows the zonal and temporal mean of vertical velocity. Two areas exhibit strong updrafts: 1) over the upwind slope of the mountain and 2) over the lee slope of the mountain centered at $y = 8$ km, $z = 5$ km. In the downstream region away from the mountain, the averaged vertical velocity oscillates between positive and negative velocities, suggesting the presence of mountain-induced gravity waves. Those stationary updrafts and downdrafts weaken with distance away from the mountain and are confined below the tropopause, indicating these lee waves are trapped, or at least partially trapped. The zonal and temporal mean of water vapor tendency due to microphysics ($\dot{q}$) is shown in Fig. 3b. The negative $\dot{q}$ value indicates condensation and deposition whereas the positive $\dot{q}$ values indicate evaporation and sublimation. Hereafter, the sum of the condensation rates and the deposition rates is referred as to as the condensation-and-deposition rates. The areas that exhibit strong updrafts also show strong condensation-and-deposition rates. The two strong condensation-and-deposition centers caused by the strong stationary updrafts correspond to the two cloud centers indicated by the sum of cloud water mixing ratio (q_c) and ice mixing ratio (q_i). It is noteworthy that the two cloud centers exist throughout our simulation and are closely related to two precipitation maxima. Notably, the impacts of water vapor nudging on the two condensation-and-deposition centers have been evaluated by additional tests in which the nudging on water vapor is only applied between the left boundary at −51.2 and −17.1 km. The results exhibit similar precipitation intensity and sensitivity to warming (Fig. S2), suggesting the q_v nudging did not impact the two condensation-and-deposition centers and precipitation significantly.

As shown in Fig. 3c, the two precipitation peaks also correspond to the two regions with high mixing ratios of precipitation hydrometeors (q_p). The q_p is the sum of mixing ratio of rainwater (q_r), graupel (q_g), and snow (q_s). The high-q_p region over the lee slope of the mountain extends from the surface to the lower troposphere, suggesting that the ice phase process is not involved much in the formation of the first precipitation peak. In contrast, the high-q_p area located downstream of the mountain extends from the surface up to upper troposphere. A significant amount of graupel is found above the downstream precipitation region, indicating the involvement of the ice and mixed phase processes in the formation of the second precipitation peak.

c. *Traveling mesoscale disturbances*

The formation of the two precipitation maxima is related to the interaction between the traveling mesoscale disturbances and mountain wave–forced ascents, although their roles are different for the two precipitation maxima. The Hovmöller diagram of the zonally averaged surface precipitation shows a precipitation pattern suggesting northward traveling mesoscale disturbances (Fig. 4). The mesoscale disturbances travel northward with a period of about 2 h. In each cycle, the zonal mean precipitation features the two precipitation maxima and a rain shadow region sandwiched by the two-precipitation maxima. Notably, little-precipitation windows can be identified for every location. The little-precipitation windows suggest that precipitation maxima are not purely the result of the mean flow advection of hydrometeors produced in the two cloud formation centers in Fig. 3b. Without the superposition of the traveling mesoscale disturbances on the mean flow, little surface precipitation is generated, probably because of insufficient microphysical conversion time or evaporation when the precipitation hydrometeors fall out of cloud at a high level (Kirshbaum and Smith 2008).

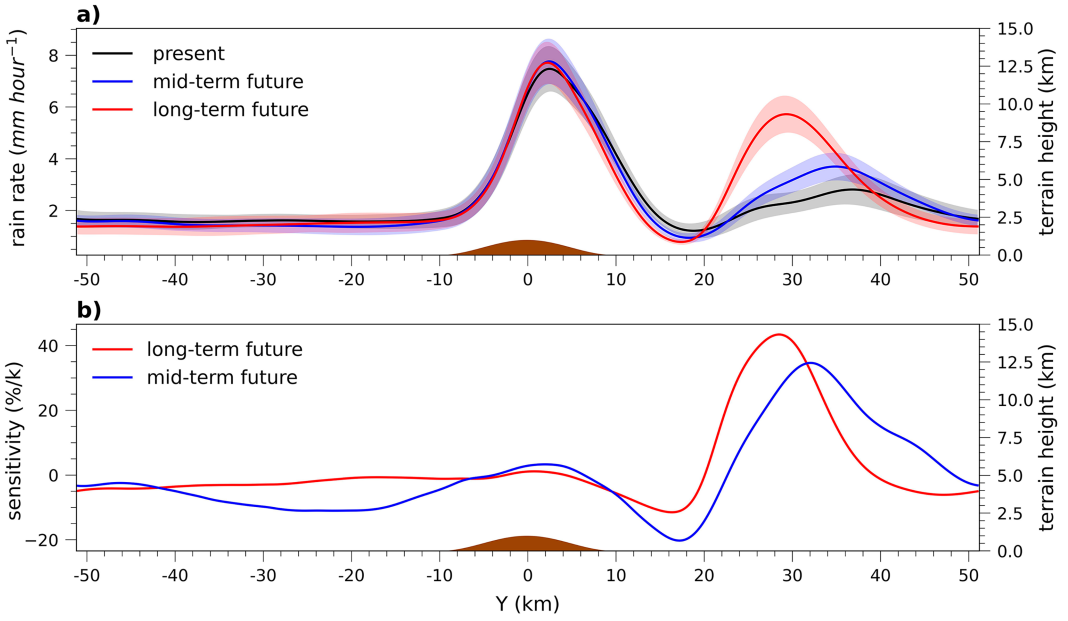

FIG. 2. (a) Zonal and temporal mean precipitation distribution in the simulations of present, midterm future, and long-term future climate. Error bars are shown as the light color shading on the curves, using two standard deviations of hourly rain rate between hour 12 and hour 36. (b) The corresponding precipitation sensitivity distribution of midterm future and long-term future climate in (a). The sensitivities in (b) are defined relative to the present climate.

To further illustrate the relations between the two condensation centers and the two precipitation maxima, regression analysis relating surface precipitation to hydrometeors (q_p, q_g, $q_i + q_c$) and $\dot{q}$ has been conducted. Following Adames and Wallace (2014), the regression map for each variable is derived from the equation, $\mathbf{D} = \mathbf{SP}^{\mathrm{T}}$, where $\mathbf{D}$ is the two-dimensional regression pattern for a two-dimensional matrix $\mathbf{S}$ that represents a variable field, and $\mathbf{P}$ is a standardized time series of the variable being regressed upon.

The precipitation maximum over the mountain is related to the interaction between the cloud above the windward slope of the mountain and the traveling mesoscale disturbances. The regressed $\dot{q}$ and $q_c + q_i$ in Fig. 5a show that low-level cloud formation is enhanced when there is a positive precipitation anomaly over the mountain. Noting that the regressed pattern represents anomalies to be added to the stationary pattern in Fig. 3 when there is a positive precipitation anomaly on the mountain surface. Figure 5a suggests that when the mesoscale disturbance reaches the mountain it probably triggers or enhances orographic convection substantially and therefore enhances surface precipitation.

Meanwhile, the regression of precipitation hydrometeors (Fig. 5b) shows a second center of positive anomaly at about 9 km above the surface and 30 km upstream of the mountain. The upper-level q_p anomaly extends downward until reaching the freezing level, but it also extends downwind and connects with the low-level cloud and precipitation. Therefore, the formation of effective precipitation over the mountain is likely also affected by the seeder–feeder mechanism (Bergeron 1960). The upper-level regression anomaly in Fig. 5b suggests stratiform precipitation in the upper and middle troposphere related to deep convective system falls from above and enhances accretion in the low-level orographic cloud above then windward slope. This regression pattern feature is also consistent with Fig. 4, which shows that the precipitation over the mountain becomes notable before the main traveling precipitation system reaches the mountain. The reason for which no deep convection signal exists upstream of the mountain (from $y = -30$ to -20 km) in the regression pattern is probably because the regression has zero time lag, which makes the regressed pattern more representative for features when precipitation over the mountain is maximized.

Figure 6 shows the regressed fields related to the precipitation in the downstream region, which suggests the interaction between cloud induced by the midtropospheric orographic ascent above the lee slope of the mountain (Fig. 3a) and the traveling convective system. The negative anomaly of regressed $\dot{q}$ and positive anomaly of regressed $q_c + q_i$ in Fig. 6a suggests that deep convection exists when surface precipitation is enhanced in the downstream region. The regressed q_p in Fig. 6b shows two maxima in the downstream region, one in the lower troposphere and the other in the upper troposphere at about 8 km. The upper-level maximum is related to the local deep convection. Interestingly, the lower-level maximum is somewhat separated from the upper-level maximum, suggesting there is an additional mechanism that enhances the lower-level precipitation hydrometeor mixing ratio. The presence of midtroposphere ascent and cloud formation above the lee slope of the mountain (Fig. 3b) can produce a significant amount of precipitation hydrometeors that drift downstream with the mean flow. As those

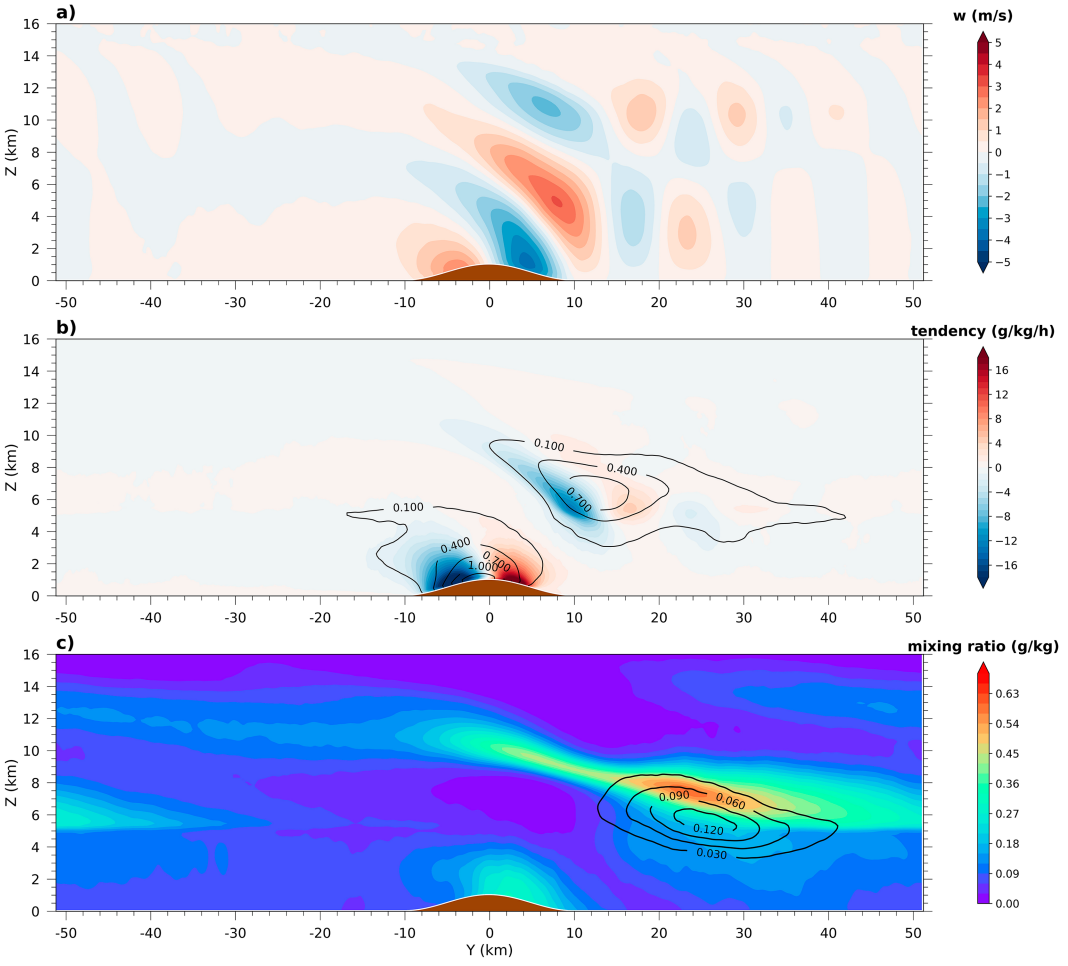

FIG. 3. Zonal and temporal means of (a) vertical velocity (w), (b) water vapor mixing ratio tendency due to microphysics (color shading), the sum of cloud ice (q_i) and cloud water (q_c) mixing ratio (contours; unit: g kg^{-1}), and (c) mixing ratio of precipitation hydrometeors which include rain, graupel, and snow (color shading) and the graupel mixing ratio alone (contours; unit: g kg^{-1}).

hydrometeors fall into the lower and middle part of the convective system that develops in the downwind region, they enhance collision-and-coalescence or accretion as in the conventional seeder–feeder mechanism. We call this mechanism the pseudo seeder–feeder (PSF) mechanism because here convection and terrain forced ascents play roles differing from what they have in the conventional seeder–feeder mechanism. The PSF mechanism is likely more important to local precipitation enhancement in the downwind region than over the mountain because the regression of graupel mixing ratio onto the second precipitation

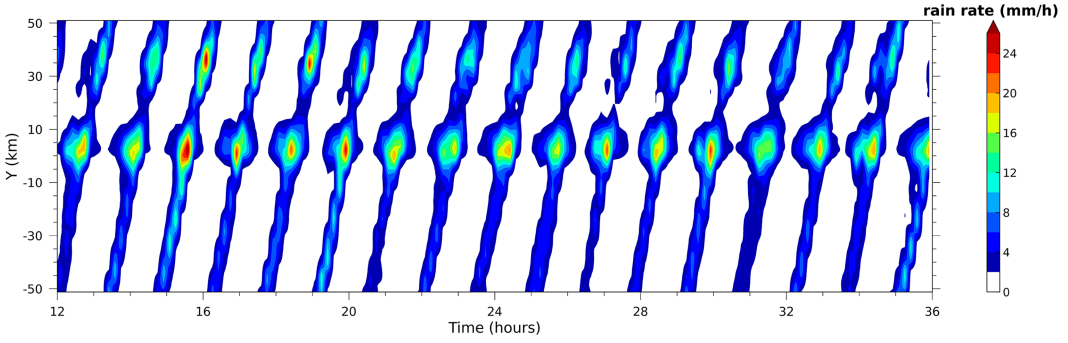

FIG. 4. Hovmöller diagram of the zonally averaged surface precipitation in the present climate simulation.

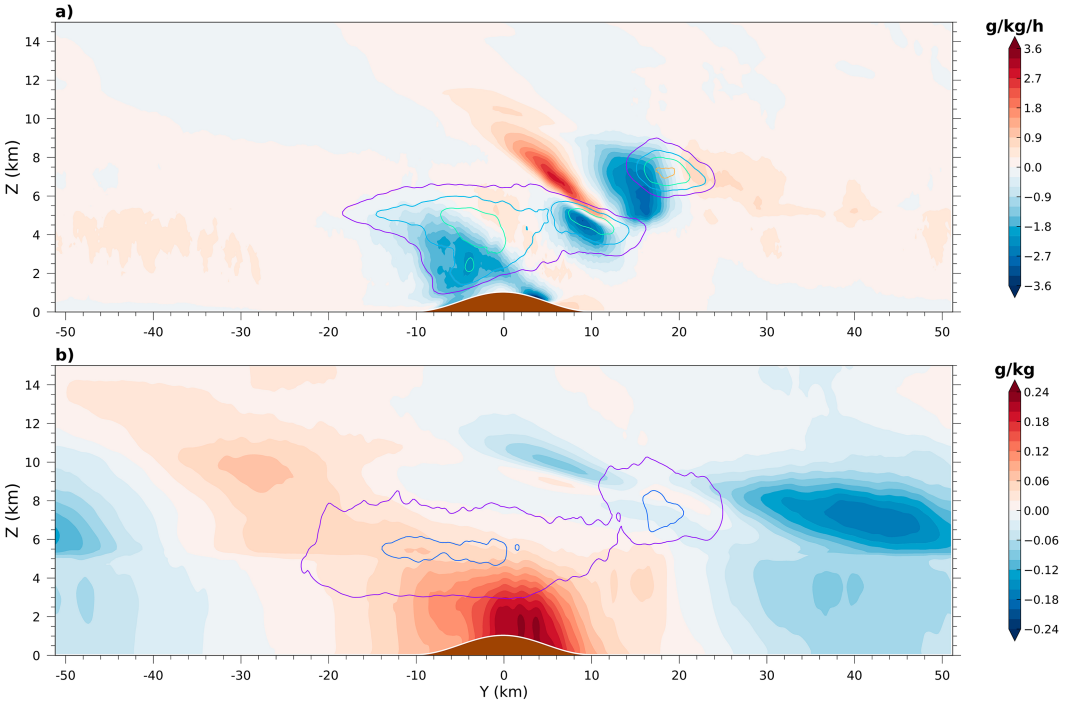

FIG. 5. (a),(b) Regression maps of water vapor tendency [$\dot{q}$; color shading in (a)], mixing ratios of ice and cloud water [$q_i + q_c$; contours in (a)], mixing ratios of precipitation hydrometeors [q_p; color shading in (b)] and mixing ratios of graupel [q_g; contours in (b)] onto the time series of mean precipitation over the mountain between $y = -14$ and 10 km in the present climate simulation. Contour interval in (a) is 0.04 g kg^{-1} and the purple contours indicate 0.04 g kg^{-1}. Contour interval in (b) is 0.01 g kg^{-1} and the purple contour indicates 0.001 g kg^{-1}.

maximum in the downstream region (Fig. 6b) exhibits a substantially stronger signal than the same regression onto the first precipitation maximum over the mountain top (Fig. 5).

4. Precipitation responses to warming

The upstream region has shown small rain rate at around 1.5 mm h^{-1} and the precipitation sensitivity is slightly negative. This negative sensitivity is not unexpected since the nonextreme precipitation should increase at a pace slower than the 2% K^{-1} rate given that extreme precipitation increases at a rate larger than the 2% K^{-1} sensitivity of global mean precipitation (e.g., Held and Soden 2006; Muller and O'Gorman 2011). In this section, we focus on the downstream region and the overmountain region, which exhibit precipitation maximum. The two regions are investigated separately to understand their responses to warming.

a. *Overmountain precipitation*

For the overmountain precipitation region, the downstream transport of hydrometeors in a strong wind environment cannot be ignored because we are considering relatively small regions. We use the black box shown in Fig. 7 for a budget analysis. The box is bounded between $y = -10$ and 14 km to include the first precipitation maximum and capped vertically at 4 km to avoid the inclusion of the lee condensation-and-deposition center in midtroposphere to which the first precipitation maximum is unrelated. The time averaged surface precipitation (P) at the bottom of this box satisfies

$$P = C_{\text{net}} + F_{\text{in}} - F_{\text{out}} + R, \tag{2}$$

where C_{net} is the volume integrated rate of net condensation and deposition, F_{in} (F_{out}) is the flux of condensates, including both nonprecipitation and precipitation particles, into (leaving) the box through upstream (downstream) boundaries. Note that C_{net}, F_{in}, and F_{out} are normalized with the bottom surface area of the box. Here R denotes the residual term due to ignoring surface evaporation, storage of hydrometeors in the air, and condensed water falling into the box from above. This residual term can be minimized when we take the time average of a relatively long period so that the storage of hydrometeors in the air can be ignored. Surface evaporation is also ignored because of its little contribution. The residual term only accounts for around 5% of the surface precipitation (Table S1), suggesting the approximate balance between P and $C_{\text{net}} + F_{\text{in}} - F_{\text{out}}$ inside the box. Including the influx of hydrometeors from upwind direction into the box, the PE is redefined as

$$\text{PE} = \frac{P}{F_{\text{in}} + C}, \tag{3}$$

where F_{in} is influx convergence into the box and C is the volume integrated rate of condensation and deposition inside the

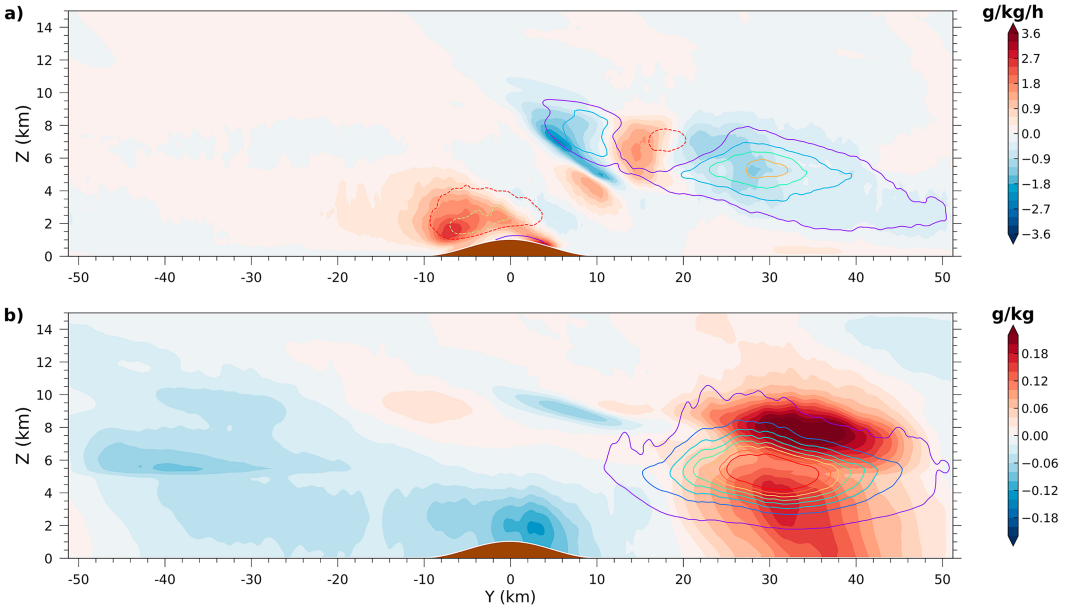

FIG. 6. As in Fig. 5, except that the variables are regressed onto the time series of the mean precipitation in the downstream region between $y = 21$ km and $y = 45$ km.

box. Both C and F_{in} are normalized with the bottom surface area of the box. For this overmountain precipitation region, C is much larger than F_{in}. Denoting the surface temperature by T_s, the total precipitation sensitivity can be decomposed as

$$\frac{1}{P}\frac{\partial P}{\partial T_s} = \frac{\partial \ln P}{\partial T_s} = \frac{\partial \ln[\mathrm{PE} \times (C + F_{in})]}{\partial T_s} = \frac{\partial \ln(C + F_{in})}{\partial T_s} + \frac{\partial \ln(\mathrm{PE})}{\partial T_s} = \frac{\partial (C + F_{in})}{(C + F_{in})\partial T_s} + \frac{\partial \mathrm{PE}}{\mathrm{PE}\,\partial T_s}. \quad (4)$$

The precipitation sensitivity over the mountain is the sum of the sensitivity of $C + F_{in}$ and that of PE. Table 1 is the average sensitivity obtained by comparing the simulations of present and midterm future and that by comparing those of present and long-term future. As shown in Table 1, both terms have shown sensitivities less than 1% K^{-1}. Therefore, the weak precipitation response to warming is due to small sensitivities of PE, F_{in}, and C. The C in the black box has shown a slight decrease with warming. This negative sensitivity is at odds with the expected positive sensitivity in previous studies (e.g., Siler and Roe 2014). To understand the negative condensation sensitivity to the warming, the change of C in the black box is further decomposed to thermodynamic and dynamic contributions based on the methodology in Shi and Durran (2015). The thermodynamic contribution is related to the change in the moist adiabatic lapse rate of saturation water vapor specific humidity (γ) due to temperature increase, and the dynamic contribution is related to

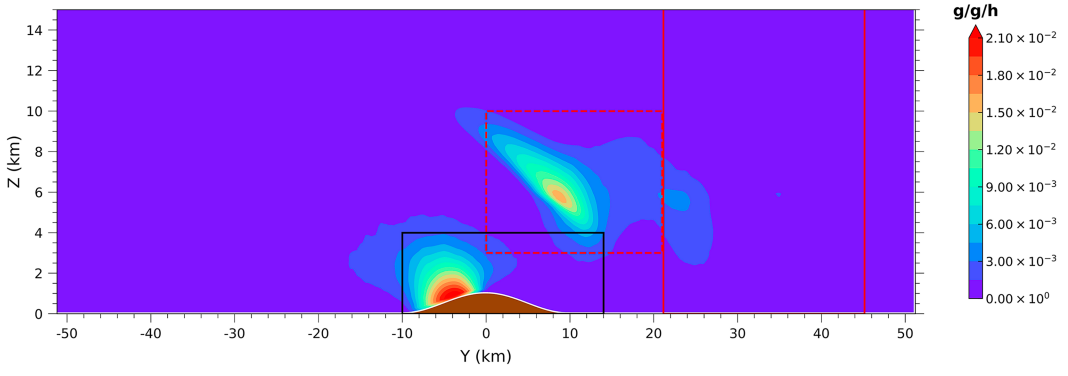

FIG. 7. Zonal and temporal mean of the sum of condensation and deposition rates in the simulation of midterm future climate. The black box over the mountain is for the analysis of precipitation maximum over the mountain, and the region bounded by red lines between $y = 21$ km and $y = 45$ km is for the analysis of precipitation over the downstream region. The red box between $y = 0$ km and $y = 21$ km wraps the condensation-and-deposition center in the lee of mountain.

TABLE 1. Sensitivity with respect to surface warming over the mountain region (indicated by the black solid box in Fig. 7): precipitation (P), the sum of condensation and deposition rates (C), flux into the black solid box from the upstream boundary (F_{in}), and precipitation efficiency (PE). C_t is the thermodynamic contribution of C, and C_d is the dynamic contribution of C. Units are % K^{-1}.

	P	C	F_{in}	$C + F_{in}$	PE	C_t	C_d
Midterm	0.69	−0.29	0.66	−0.14	0.84	2.16	−2.55
Long-term	−1.81	−1.32	1.00	−0.97	−0.86	2.07	−2.81
Mean	−0.56	−0.80	0.83	−0.56	−0.01	2.11	−2.68

the change in the vertical velocity (Muller and Takayabu 2020; Shi and Durran 2015). Our calculation found that the thermodynamic contribution is at around 2.11% K^{-1}, which is offset by the dynamic contribution at around −2.68% K^{-1}. The temperature of the upslope condensation center in our black box ranges from ~270 to ~300 K. Our calculation of thermal contribution to the warming is consistent with the γ sensitivity in that temperature range [shown in Fig. 12 of Shi and Durran (2014)].

The negative dynamic contribution is related to the weakening of vertical velocities over the windward slope of the mountain under warming. The zonal and temporal mean of vertical velocities are shown in Fig. 8. The mean vertical velocity maximum over the windward slope of the mountain does not exhibit appreciable change but the depth of the ascending layer becomes shallower in response to warming. The weakening of vertical velocities (Fig. S3) is probably related to the response of mountain wave to the increased stability (Shi and Durran 2015), which is caused by the amplified warming in the upper troposphere. Additionally, a negative dynamic contribution is also found in the previous study of extreme convective precipitation in the tropics (Muller et al. 2011).

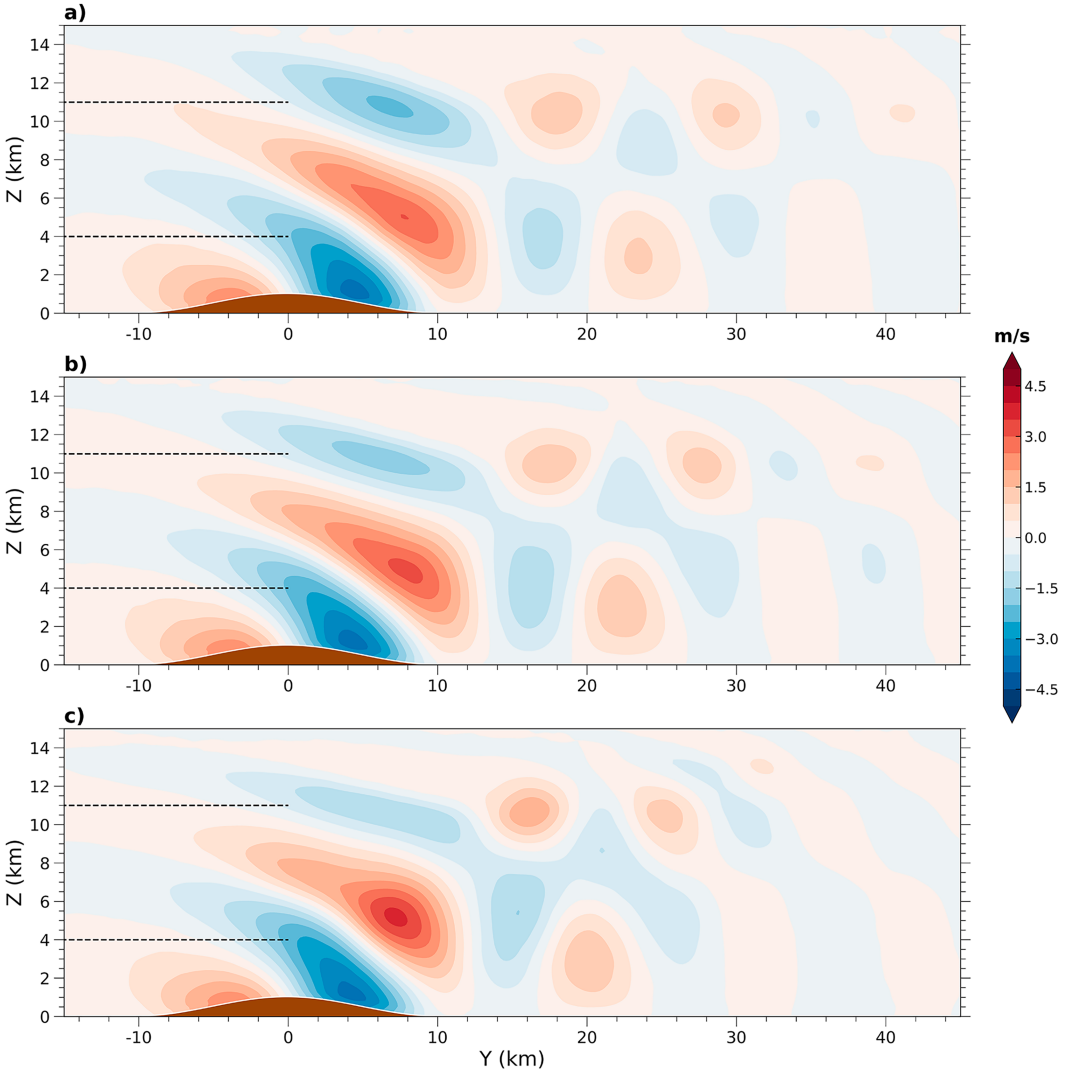

FIG. 8. Zonal and temporal mean of vertical velocities of simulations of the climate of the (a) present, (b) midterm future, and (c) long-term future. The black dashed lines at 4 and 11 km are for height references.

TABLE 2. Sensitivity with respect to surface warming in the downstream region (indicated by the red solid box in Fig. 7): precipitation (P), condensation (C), flux into the red solid box from the upstream boundary (F_{in}), precipitation efficiency (PE). The term C_2 is the condensation rate of the red dashed box region shown in Fig. 7. C_{2t} is the thermodynamic contribution of C_2, and C_{2d} is the dynamic contribution of C_2. Units are % K^{-1}.

	P	C	F_{in}	$C + F_{in}$	PE	C_2	C_{2t}	C_{2d}
Midterm	19.37	−0.83	12.02	6.32	12.14	11.52	7.99	1.29
Long-term	16.96	−1.42	6.49	2.46	13.34	6.80	6.41	0.79
Mean	18.16	−0.29	9.25	4.39	12.74	9.16	7.20	1.04

b. *Downstream-region precipitation*

In the downstream precipitation maximum region, we conduct the same budget analysis for precipitation efficiency and hydrometeor production. The budget box is defined starting from 21 to 45 km in the y direction, which is indicated by the red solid vertical lines in Fig. 7. The downstream precipitation statistics are partly shown in Table S2.

The precipitation in the downstream has exhibited substantial change due to warming and, as shown in Table 2, the mean precipitation sensitivity is at 18.16% K^{-1}. The local C has exhibited little change and its mean sensitivity to the warming is at −0.29% K^{-1}. In contrast, the F_{in} sensitivity is at 9.25% K^{-1}, suggesting the increased influx with warming. The F_{in} increase can be explained by the increased condensation and deposition rate in the lee-slope midtroposphere condensation-and-deposition center C_2 (denoted by the red dashed box in Fig. 7). The sensitivities of C_2 are consistent with the F_{in} (Table 2), indicating that the influx increase is due to the amplification of C_2. We further decompose the change of the C_2 into thermodynamic and dynamic contributions. The dynamic contribution is slightly positive and at 1.04% K^{-1}, while the thermodynamic contribution is at 7.20% K^{-1}, revealing that the increase of influx is primarily from thermodynamic contribution. The thermodynamic sensitivity of C_2 is larger than that of the low-level windward slope condensation center because 1) the sensitivity of γ to temperature is higher at colder temperatures [Fig. 12 of Shi and Durran (2014)] and 2) the midtroposphere exhibits a larger temperature increase than the surface. The height dependence of the thermodynamic condensation sensitivity is also highlighted in Siler and Roe (2014). Compared to the overmountain region where dynamic condensation sensitivity is negative and the PE remain nearly constant, the downstream precipitation sensitivity is further increased by the positive dynamic condensation sensitivity of the lee condensation-and-deposition center and increased PE.

Following Eq. (4), the precipitation sensitivity in the downstream region can also be decomposed into the sensitivity related to PE change and source of hydrometeors ($C + F_{in}$). The change in PE is dominant at 12.74% K^{-1}, while the change of the sum of local condensation and influx plays a secondary role at 4.39% K^{-1} (Table 2). The high PE sensitivity suggests enhancement of the pseudo seeder–feeder effects. This enhancement is probably due to the increases of F_{in} into the downstream region that can be further attributed to the amplified lee cloud formation center C_2.

The high precipitation peak sensitivity in the downstream region is also partially due to the upwind shift of the second precipitation maximum, which exhibits ~10 km between the present and long-term future simulations. This upwind shift of downstream-region precipitation peak is related to the upwind shift of mean state mountain waves and the lifting of freezing level in the warmed climates. The mean state wave patterns of vertical velocities are shown in Fig. 8. The updraft centered at $y \approx 24$ km in the simulation of present climate moves upwind to $y \approx 20$ km in the simulation in of long-term future climate. With the upwind shift of mean state waves, the region which is prone to the development of new convection in the downstream region moves upwind. The hydrometeors drifting from the lee midtroposphere center will travel at a shorter distance and experience less evaporation or sublimation before seeding the low-level convection in the downstream region. In addition, as the freezing level shifts upward, the fraction of liquid-phase hydrometeors increases in the lee slope midtroposphere cloud center. As a result, the seeder hydrometeors fall at relatively larger terminal velocity and tend to interact with the low-level feeder clouds earlier at a shorter travel distance in the horizontal direction.

5. Upwind shift of trapped lee waves

The upwind shift of downstream precipitation maximum is, at least partially, related to the upwind shift of trapped lee waves, which is investigated in this section with the numerical methods of Durran et al. (2015), which search for linear modes that represent trapped waves in the lee of a mountain.

We used a three-layer setup for the linear model, with layer interfaces at 9 and 16 km for the present climate, and 10 and 17 km for the long-term future climate. The higher interfaces in the future climate are expected because the global warming leads to the lifting of tropopause height (e.g., Lin et al. 2017). The moist squared Brunt–Väisälä frequency N^2 for the present climate setup is 1.2, 0.5, and 5×10^{-4} s^{-2} for the three layers from bottom to top. For the long-term future scenario, the mid-layer N^2 increases from 0.5×10^{-4} to 0.8×10^{-4} s^{-2}. The N^2 in other layers is the same as the present climate setup. The horizontal wind is assumed as 20 m s^{-1} at all layers in both climates. This assumption of the wind profile is the main caveat that we cannot avoid because in three-dimensional CM1 simulations we have both u and v velocity components, but we can only have one horizontal direction in the two-dimensional model. These parameters are idealizations based on the simulation data. The method of Durran et al. (2015) yields two trapped modes for each setup. However, one of them has only one vertical velocity extremum in the troposphere and is not consistent with the mean velocity pattern in Fig. 8.

The relevant solution of the trapped model for the present climate (future climate) is shown in Fig. 9a (Fig. 9b). The oscillation pattern of normalized vertical velocities in Figs. 9a and 9b shows upwind shift of the trapped lee waves. The upwind shift of trapped lee waves is due to the decrease in the horizontal wavelength of trapped lee waves. The resonant wavelength decreases

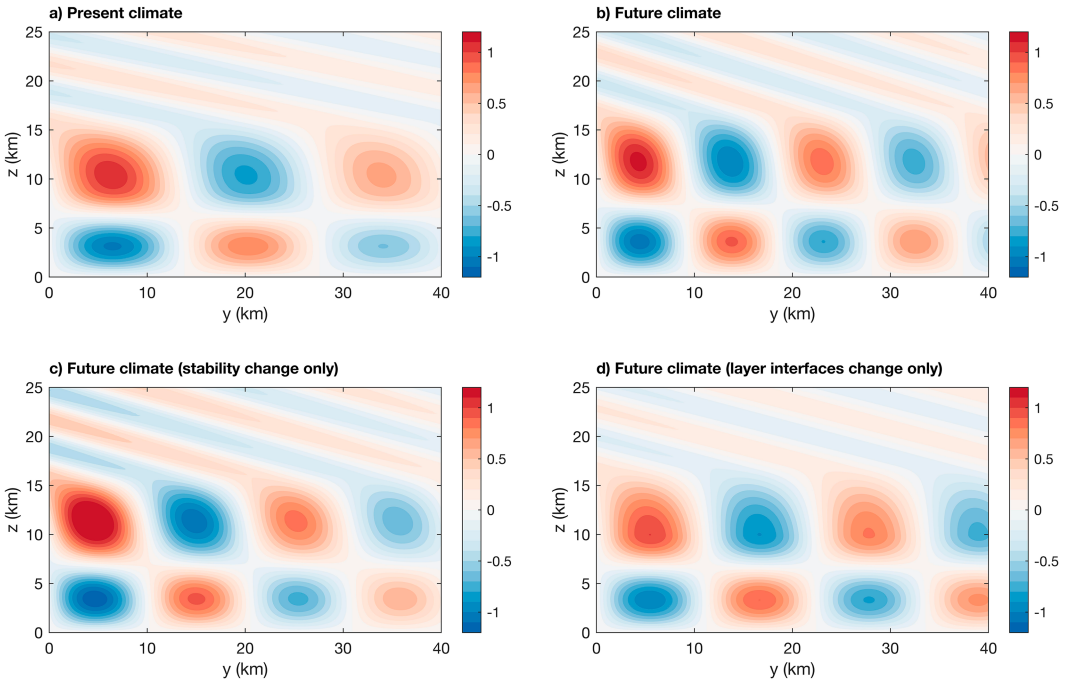

FIG. 9. Contours of normalized vertical velocities in a vertical cross section obtained using the numerical methods developed by Durran et al. (2015). (a) Calculations based on the stability parameters and the layer interfaces of the present climate. (b) Calculations based on the stability parameters and the layer interfaces of the long-term future climate. (c) Calculations based on the stability parameters of the long-term future climate but the layer interfaces of present climate. (d) Calculations based on the stability parameters of the present climate but the layer interfaces of the long-term future climate.

from the 27.6 km in the present climate setup to the 18.7 km in the long-term future climate setup. The effects of increased upper troposphere (the middle layer in the three-layer setup) static stability and lifted layer interfaces are separately evaluated. Figure 9c shows the future climate with increased stability only, while Fig. 9d shows the future climate with lifted layer interfaces only. Both factors contribute to the decrease of the resonant wavelength. If we only change the stability N^2 while keeping the layer interface heights unchanged, the resonant wavelength decreases to 20.4 km. If the layer interfaces are changed while the stability is kept constant, the resonant wavelength decreases to 22.1 km. Therefore, the stability enhancement is probably more important to induce the upwind shift of trapped lee waves, although the role of lifted layer interfaces is also nonnegligible.

6. Robustness of results

The robustness of our results is tested using the Morrison microphysics scheme, a narrower mountain with half-width of 5 km (NM) and different mountain heights.

a. *Microphysics schemes*

Figure 10a shows the zonal and temporal rainfall distribution in the simulations using the Morrison microphysical scheme. Different from the Thompson scheme, the second precipitation maximum downstream of the mountain in Morrison is weak and virtually nonexistent. The discrepancy in the occurrence of precipitation maxima in the downstream region in the simulation of present climate is probably related to the different liquid to solid ratios of the seeder particles in these two microphysical schemes. The transition of seeding precipitation particles from the solid phase to the liquid phase happens in an earlier stage in the Morrison scheme (Fig. S4). As a result, a higher liquid ratio in the seeding precipitation particles is expected in the Morrison scheme. Given the ice particles involved processes are more efficient in producing rainwater (Kirshbaum and Smith 2008), the PSF in the Morrison scheme is expected to be weaker and thus may fail to create the downstream precipitation peak. In addition, the greater sensitivities exhibited by the Morrison simulations in the windward side are also likely related to the different representations of mixed-phase processes in microphysics schemes, whose impact will be investigated in a future study.

b. *Mountain width*

Experiments using a narrower mountain with a half-width of 5 km (NM) are also tested with different microphysical schemes. Previous experiments using the 10-km mountain half-width are referred to as the wide mountain (WM). The two cloud formation centers induced by the NM are much smaller (Fig. S4). With smaller cloud formation centers, both the traditional seeder–feeder effects and PSF are weakened and therefore weaker precipitation results in the NM simulations (shown in Figs. 10a,c). Interestingly, in the present climate of NM, both microphysics schemes do not produce the downstream precipitation maximum.

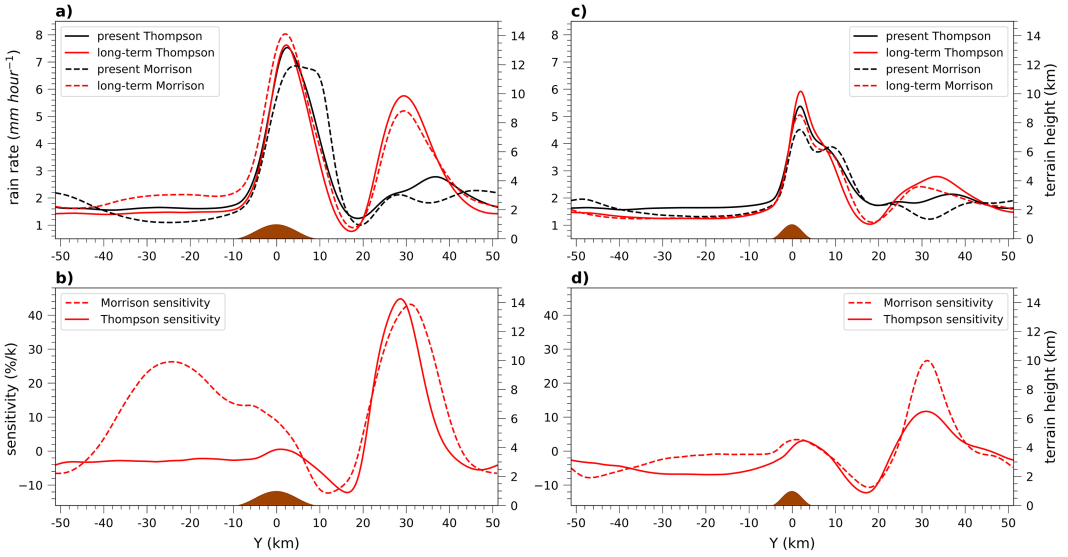

FIG. 10. (a) Temporal and zonal mean precipitation in the simulation of present and long-term future climate and (b) corresponding precipitation sensitivity using different half-widths of the mountain range and microphysical schemes. The half-width of 10 km using the Thompson and Morrison schemes. (c),(d) The half-width of 5 km using the Thompson scheme and Morrison schemes.

This is probably because the weaker lee cloud formation center supplies fewer drifting hydrometeors that serve as seeder particles in PSF. Although the solid particle fraction in present climate is higher than that in warmed climates, this advantageous condition for enhanced PSF is outweighed by the weaker lee cloud formation center in the present climate.

c. *Mountain heights*

Simulations with different mountain heights are conducted. We consider two ideal mountain setups, a high mountain with maximum height of 2 km (HM) and a lower mountain with 0.5 km (LM). HM experiments exhibit substantially stronger precipitation peaks than LM experiments (Figs. 11a,b) because of stronger vertical motions in the upslope and leeside midtroposphere cloud centers in the HM experiments (Fig. S5). The HM experiments in the present climate shows a downstream rainfall peak close to the overmountain peak (Fig. 11b), suggesting a highly efficient PSF effect with very strong lee condensation-and-deposition center. However, the downstream precipitation maximum region (defined as region between $y = 11$ and 32 km) for HM experiments has low sensitivity at around 2.51% K^{-1}, indicating that the amplified lee condensation-and-deposition center under warming does not substantially enhance the downstream PE, probably because the PSF is already intense and efficient and approaches its limit in enhancing PE in the present climate.

7. Conclusions

The global warming response of orographic precipitation induced by the interaction between a typhoon's outer circulation environment and a mountain is estimated with pseudo–global warming experiments using LES. In our control simulation for the present climate, the cross-mountain direction precipitation distribution exhibits two maxima with the first maximum located on the lee slope of the mountain and the second weaker maximum in the region downstream of the mountain. The first precipitation maximum is related to the conventional seeder–feeder effect and enhanced convection by the mountain. The second maximum is related to a pseudo seeder–feeder effect in which the seeder cloud is the mountain wave–induced midtroposphere cloud above the lee slope and the feeder cloud is the middle and lower parts of traveling precipitation system in the downstream region.

In response to the warming, the first rainfall maximum exhibits almost no change because both condensation rate and precipitation efficiency have negligible changes. This weak sensitivity of condensation rate is because the positive thermodynamic contribution is canceled by the negative dynamic contribution. In contrast, the second rainfall maximum shifts upwind and intensifies significantly. The precipitation sensitivity in the downstream region (21–45 km away from mountain) is at 18.16% K^{-1} on average and has a maximum sensitivity up to 43.41% K^{-1}. This accelerated rainfall intensification is attributed to the substantial amplification of the condensation-and-deposition center in the midtroposphere above the lee slope, where the temperature is lower than the low-level condensation center and the thermodynamic sensitivity is relatively high. This enhancement increases the downstream precipitation by increasing the influx of hydrometeors and thereby enhancing the pseudo seeder–feeder effect.

The high peak sensitivity in the downstream-region precipitation is also partially due to the upwind shift of the precipitation maximum, which is caused by the upwind shift of the trapped lee waves and the lifting of the freezing level. The upwind shift of trapped lee waves is further corroborated by a three-layer linear mountain wave model, which shows a

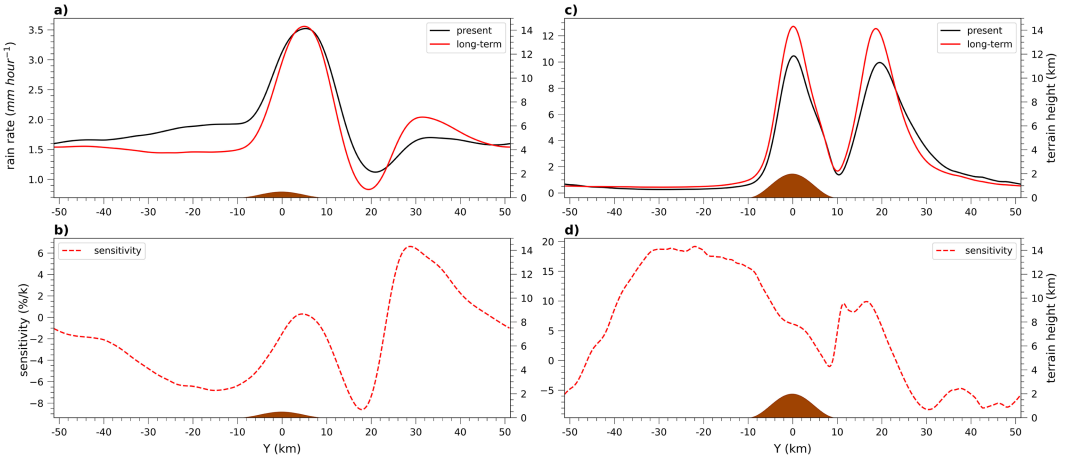

FIG. 11. Temporal and zonal mean precipitation in the simulation of present and long-term future climate, and corresponding precipitation sensitivity using mountain maximum height of (a),(b) 0.5 and (c),(d) 2 km. The microphysical scheme used is the Thompson scheme.

decrease in the resonant wavelength of the trapped lee wave due to the lifted layer interfaces and the increased upper tropospheric stability under warming.

The robustness of our results is tested with idealized mountains with different mountain heights and widths and a different microphysics scheme. Consistently, all simulations in the warmed climate show upwind shift and intensification of the downstream precipitation maximum. However, the magnitude of downstream precipitation sensitivity varies significantly. This is because the downstream PE sensitivity is restricted by the activation and amplification of PSF which are further regulated by magnitude of the lee condensation-and-deposition center. If the lee condensation-and-deposition center is too weak (e.g., the NM experiments), the PSF may not be activated. If the lee condensation-and-deposition center is too strong (the HM experiments), its enhancement under warming may not further enhance PSF-related PE, probably because the drifting seeder particles are overly sufficient. In addition, the comparison between different microphysics schemes highlights that the increased liquid to solid ratio under warming may weaken the PSF.

This study focuses on a typhoon environment. However, based on additional simulations, it is suggested that the general applicability of the phenomenon can be extended to other similar environments characterized by strong winds and highly moist environments. The high wind speed allows the formation of strong mountain waves and a strong lee cloud center in the midtroposphere. The very moist environment allows the convective system to be triggered and developed. The strong wind and highly moist environment are necessary conditions for the activation of the PSF. The lee condensation-and-deposition center is too weak to activate the PSF in the environment of weak wind speed, while no convective system can be developed if the environment is not moist enough.

Our estimation of future orographic precipitation in the typhoon outer region environment shows that the greatest precipitation sensitivity may happen in the downstream area. Although these are idealized experiments, our findings suggest plausible mechanisms by which the precipitation maximum in the downstream region of mountain barriers may emerge and intensify substantially under warming. Those mechanisms warrant further investigations focusing on the downstream region of mountains in the context of flooding risk management under climate change.

Acknowledgments. The authors thank four anonymous reviewers for their constructive comments. This research was supported by the Research Grants Council of Hong Kong SAR, China (Projects AoE/E-603/18 and HKUST 26305720) and the Center for Ocean Research in Hong Kong and Macau (CORE), a joint research center between the Qingdao National Laboratory for Marine Science and Technology (QNLM) and the Hong Kong University of Science and Technology (HKUST). The authors thank HKUST Fok Ying Tung Research Institute and National Supercomputing Center in Guangzhou Nansha subcenter for providing high-performance computational resources.

Data availability statement. The CM1 code and namelist files can be found at https://github.com/JiananChenUST/Chen-and-Shi-2023-.git. The initial input profiles are also included.

REFERENCES

Adames, Á. F., and J. M. Wallace, 2014: Three-dimensional structure and evolution of the MJO and its relation to the mean flow. *J. Atmos. Sci.*, **71**, 2007–2026, https://doi.org/10.1175/JAS-D-13-0254.1.

Ardeshiri, H., M. Cassiani, S. Y. Park, A. Stohl, I. Pisso, and A. S. Dinger, 2020: On the convergence and capability of the large-eddy simulation of concentration fluctuations in passive plumes for a neutral boundary layer at infinite Reynolds number. *Bound.-Layer Meteor.*, **176**, 291–327, https://doi.org/10.1007/s10546-020-00537-6.

Beniston, M., 2005: Mountain climates and climatic change: An overview of processes focusing on the European Alps. *Pure*

Appl. Geophys., **162**, 1587–1606, https://doi.org/10.1007/s00024-005-2684-9.

Bergeron, T., 1960: Problems and methods of rainfall investigation:Address of the honorary chairman of the conference. *Physics of Precipitation*, *Geophys. Monogr.*, Vol. 5, Amer. Geophys. Union, 5–30.

Bryan, G. H., and J. M. Fritsch, 2002: A benchmark simulation for moist nonhydrostatic numerical models. *Mon. Wea. Rev.*, **130**, 2917–2928, https://doi.org/10.1175/1520-0493(2002)130<2917:ABSFMN>2.0.CO;2.

——, J. C. Wyngaard, and J. M. Fritsch, 2003: Resolution requirements for the simulation of deep moist convection. *Mon. Wea. Rev.*, **131**, 2394–2416, https://doi.org/10.1175/1520-0493(2003)131<2394:RRFTSO>2.0.CO;2.

——, R. P. Worsnop, J. K. Lundquist, and J. A. Zhang, 2017: A simple method for simulating wind profiles in the boundary layer of tropical cyclones. *Bound.-Layer Meteor.*, **162**, 475–502, https://doi.org/10.1007/s10546-016-0207-0.

Carlson, T. N., and F. E. Boland, 1978: Analysis of urban-rural canopy using a surface heat flux/temperature model. *J. Appl. Meteor.*, **17**, 998–1013, https://doi.org/10.1175/1520-0450(1978)017<0998:AOURCU>2.0.CO;2.

Chen, X., G. H. Bryan, J. A. Zhang, J. J. Cione, and F. D. Marks, 2021: A framework for simulating the tropical-cyclone boundary layer using large-eddy simulation and its use in evaluating PBL parameterizations. *J. Atmos. Sci.*, **11**, 3559–3574, https://doi.org/10.1175/JAS-D-20-0227.1.

Chow, F. K., C. Schär, N. Ban, K. A. Lundquist, L. Schlemmer, and X. Shi, 2019: Crossing multiple gray zones in the transition from mesoscale to microscale simulation over complex terrain. *Atmosphere*, **10**, 274, https://doi.org/10.3390/atmos10050274.

Deardorff, J. W., 1980: Stratocumulus-capped mixed layers derived from a three-dimensional model. *Bound.-Layer Meteor.*, **18**, 495–527, https://doi.org/10.1007/BF00119502.

Douville, H., S. Qasmi, A. Ribes, and O. Bock, 2022: Global warming at near-constant tropospheric relative humidity is supported by observations. *Commun. Earth Environ.*, **3**, 237, https://doi.org/10.1038/s43247-022-00561-z.

Durran, D. R., M. O. G. Hills, and P. N. Blossey, 2015: The dissipation of trapped lee waves. Part I: Leakage of inviscid waves into the stratosphere. *J. Atmos. Sci.*, **72**, 1569–1584, https://doi.org/10.1175/JAS-D-14-0238.1.

Guichard, F., and F. Couvreux, 2017: A short review of numerical cloud-resolving models. *Tellus*, **69A**, 1373578, https://doi.org/10.1080/16000870.2017.1373578.

Held, I. M., and B. J. Soden, 2006: Robust responses of the hydrological cycle to global warming. *J. Climate*, **19**, 5686–5699, https://doi.org/10.1175/JCLI3990.1.

Hong Kong Observatory, 2012: Report on severe Typhoon Vicente. Accessed 10 December 2022, https://www.hko.gov.hk/en/informtc/vicente/vicente.htm.

Houze, R. A., Jr., 2012: Orographic effects on precipitating clouds. *Rev. Geophys.*, **50**, RG1001, https://doi.org/10.1029/2011RG000365.

Iacono, M. J., J. S. Delamere, E. J. Mlawer, M. W. Shephard, S. A. Clough, and W. D. Collins, 2008: Radiative forcing by long-lived greenhouse gases: Calculations with the AER radiative transfer models. *J. Geophys. Res.*, **113**, D13103, https://doi.org/10.1029/2008JD009944.

Jing, X., B. Geerts, Y. Wang, and C. Liu, 2019: Ambient factors controlling the wintertime precipitation distribution across mountain ranges in the interior western United States. Part II: Changes in orographic precipitation distribution in a pseudo–global warming simulation. *J. Appl. Meteor. Climatol.*, **58**, 695–715, https://doi.org/10.1175/JAMC-D-18-0173.1.

Ji, F., and Coauthors, 2020: Projected changes in vertical temperature profiles for Australasia. *Climate Dyn.*, **55**, 2453–2468, https://doi.org/10.1007/s00382-020-05392-2.

Kirshbaum, D. J., and R. B. Smith, 2008: Temperature and moist-stability effects on midlatitude orographic precipitation. *Quart. J. Roy. Meteor. Soc.*, **134**, 1183–1199, https://doi.org/10.1002/qj.274.

——, B. Adler, N. Kalthoff, C. Barthlott, and S. Serafin, 2018: Moist orographic convection: Physical mechanisms and links to surface-exchange processes. *Atmosphere*, **9**, 80, https://doi.org/10.3390/atmos9030080.

Lin, P., D. Paynter, Y. Ming, and V. Ramaswamy, 2017: Changes of the tropical tropopause layer under global warming. *J. Climate*, **30**, 1245–1258, https://doi.org/10.1175/JCLI-D-16-0457.1.

Lin, Y.-L., R. L. Deal, and M. S. Kulie, 1998: Mechanisms of cell regeneration, development, and propagation within a two-dimensional multicell storm. *J. Atmos. Sci.*, **55**, 1867–1886, https://doi.org/10.1175/1520-0469(1998)055<1867:MOCRDA>2.0.CO;2.

Mallen, K. J., M. T. Montgomery, and B. Wang, 2005: Reexamining the near-core radial structure of the tropical cyclone primary circulation: Implications for vortex resiliency. *J. Atmos. Sci.*, **62**, 408–425, https://doi.org/10.1175/JAS-3377.1.

Matheou, G., and D. Chung, 2014: Large-eddy simulation of stratified turbulence. Part II: Application of the stretched-vortex model to the atmospheric boundary layer. *J. Atmos. Sci.*, **71**, 4439–4460, https://doi.org/10.1175/JAS-D-13-0306.1.

Morrison, H., G. Thompson, and V. Tatarskii, 2009: Impact of cloud microphysics on the development of trailing stratiform precipitation in a simulated squall line: Comparison of one- and two-moment schemes. *Mon. Wea. Rev.*, **137**, 991–1007, https://doi.org/10.1175/2008MSWR2556.1.

Muller, C. J., 2013: Impact of convective organization on the response of tropical precipitation extremes to warming. *J. Climate*, **26**, 5028–5043, https://doi.org/10.1175/JCLI-D-12-00655.1.

——, and P. A. O'Gorman, 2011: An energetic perspective on the regional response of precipitation to climate change. *Nat. Climate Change*, **1**, 266–271, https://doi.org/10.1038/nclimate1169.

——, and Y. Takayabu, 2020: Response of precipitation extremes to warming: What have we learned from theory and idealized cloud-resolving simulations, and what remains to be learned? *Environ. Res. Lett.*, **15**, 035001, https://doi.org/10.1088/1748-9326/ab7130.

——, P. A. O'Gorman, and L. E. Back, 2011: Intensification of precipitation extremes with warming in a cloud-resolving model. *J. Climate*, **24**, 2784–2800, https://doi.org/10.1175/2011JCLI3876.1.

O'Gorman, P. A., 2015: Precipitation extremes under climate change. *Curr. Climate Change Rep.*, **1**, 49–59, https://doi.org/10.1007/s40641-015-0009-3.

Pavelsky, T. M., S. Sobolowski, S. B. Kapnick, and J. B. Barnes, 2012: Changes in orographic precipitation patterns caused by a shift from snow to rain. *Geophys. Res. Lett.*, **39**, L18706, https://doi.org/10.1029/2012GL052741.

Rasmussen, R., and Coauthors, 2011: High-resolution coupled climate runoff simulations of seasonal snowfall over Colorado: A process study of current and warmer climate. *J. Climate*, **24**, 3015–3048, https://doi.org/10.1175/2010JCLI3985.1.

Saddoughi, S. G., and S. V. Veeravalli, 1994: Local isotropy in turbulent boundary layers at high Reynolds number. *J. Fluid Mech.*, **268**, 333–372, https://doi.org/10.1017/S0022112094001370.

Sato, T., F. Kimura, and A. Kitoh, 2007: Projection of global warming onto regional precipitation over Mongolia using a regional climate model. *J. Hydrol.*, **333**, 144–154, https://doi.org/10.1016/j.jhydrol.2006.07.023.

Schär, C., and C. Frei, 2005: Orographic precipitation and climate change. *Global Change and Mountain Regions*, U. M. Huber, H. K. M. Bugmann, and M. A. Reasoner, Eds., Advances in Global Change Research, Vol. 23, Springer, 255–266.

——, ——, D. Lüthi, and H. C. Davies, 1996: Surrogate climate-change scenarios for regional climate models. *Geophys. Res. Lett.*, **23**, 669–672, https://doi.org/10.1029/96GL00265.

Shi, X., and D. R. Durran, 2014: The response of orographic precipitation over idealized midlatitude mountains due to global increases in CO_2. *J. Climate*, **27**, 3938–3956, https://doi.org/10.1175/JCLI-D-13-00460.1.

——, and ——, 2015: Estimating the response of extreme precipitation over midlatitude mountains to global warming. *J. Climate*, **28**, 4246–4262, https://doi.org/10.1175/JCLI-D-14-00750.1.

——, and Y. Wang, 2022: Impacts of cumulus convection and turbulence parameterizations on the convection-permitting simulation of typhoon precipitation. *Mon. Wea. Rev.*, **150**, 2977–2997, https://doi.org/10.1175/MWR-D-22-0057.1.

——, F. K. Chow, R. L. Street, and G. H. Bryan, 2019: Key elements of turbulence closures for simulating deep convection at kilometer-scale resolution. *J. Adv. Model. Earth Syst.*, **11**, 818–838, https://doi.org/10.1029/2018MS001446.

Siler, N., and G. Roe, 2014: How will orographic precipitation respond to surface warming? An idealized thermodynamic perspective. *Geophys. Res. Lett.*, **41**, 2606–2613, https://doi.org/10.1002/2013GL059095.

Smith, R. B., P. Schafer, D. Kirshbaum, and E. Regina, 2009: Orographic enhancement of precipitation inside Hurricane Dean. *J. Hydrometeor.*, **10**, 820–831, https://doi.org/10.1175/2008JHM1057.1.

Soden, B. J., and I. M. Held, 2006: An assessment of climate feedbacks in coupled ocean–atmosphere models. *J. Climate*, **19**, 3354–3360, https://doi.org/10.1175/JCLI3799.1.

Takemi, T., Y. Okada, R. Ito, H. Ishikawa, and E. Nakakita, 2016: Assessing the impacts of global warming on meteorological hazards and risks in Japan: Philosophy and achievements of the SOUSEI program. *Hydrol. Res. Lett.*, **10**, 119–125, https://doi.org/10.3178/hrl.10.119.

Thompson, G., P. R. Field, R. M. Rasmussen, and W. D. Hall, 2008: Explicit forecasts of winter precipitation using an improved bulk microphysics scheme. Part II: Implementation of a new snow parameterization. *Mon. Wea. Rev.*, **136**, 5095–5115, https://doi.org/10.1175/2008MWR2387.1.

Trapp, R. J., M. J. Woods, S. G. Lasher-Trapp, and M. A. Grover, 2021: Alternative implementations of the "pseudo-global-warming" methodology for event-based simulations. *J. Geophys. Res. Atmos.*, **126**, e2021JD035017, https://doi.org/10.1029/2021JD035017.

Wang, Y., Y. Wang, and H. Fudeyasu, 2009: The role of Typhoon Songda (2004) in producing distantly located heavy rainfall in Japan. *Mon. Wea. Rev.*, **137**, 3699–3716, https://doi.org/10.1175/2009MWR2933.1.